MICHIGAN STATE UNIVERSITY

CYCLOTRON LABORATORY

PHASE SPACE DIAGRAMS FOR A MIGMA FUSION DEVICE

M. M. GORDON and D. A. JOHNSON

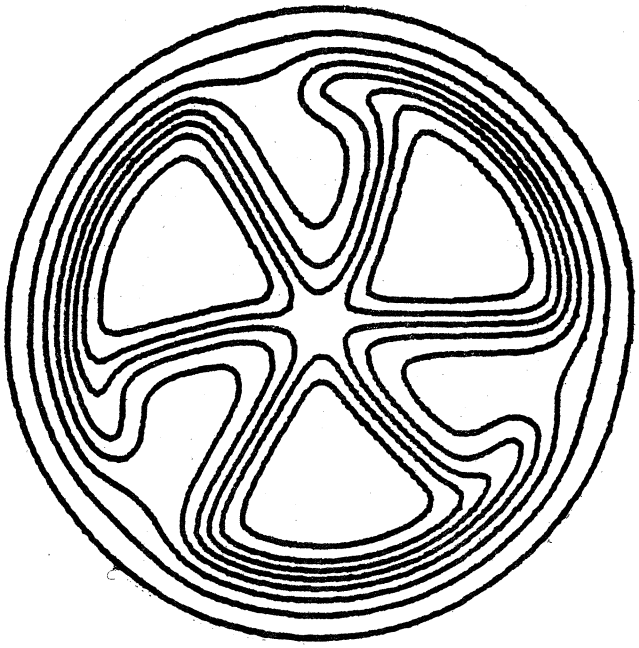

MSUCL-157 JANUARY 1975

Phase Space Diagrams for a Migma Fusion Device*

M. M. Gordon and D. A. Johnson
Cyclotron Laboratory, Physics Department,
Michigan State University, East Lansing, Michigan 48824 USA

ABSTRACT

Results are presented from a systematic study of three dimensional orbits in a Migma fusion device. As the vertical oscillation amplitude increases, the frequency of the oscillations decreases rapidly, so that a sequence of nonlinear coupling resonances are encountered. The periodic orbits and vortex boundaries associated with these resonances have been calculated, and the results are displayed in a series of phase space diagrams, together with an explanation of their significance. The vertical confinement limit and its effect on these diagrams are also described. The problems of beam injection via self-ensnaring are examined, and a special injection orbit is proposed which should provide an exceptionally long confinement time together with a high central density. Finally, the effect of multiple scattering on the ion distribution in phase space is discussed, and arguments are presented in favor of a rather broad distribution under steady state conditions.

*Work supported by the National Science Foundation.

1. Introduction

During the past few years, a group headed by B. C. Maglich has been working on the development of a practical fusion power source through the application of storage ring and colliding beam concepts.[1] A detailed report on this work was presented in a paper entitled "The Migma Principle of Controlled Fusion", in which Maglich[2] describes the theory and design of the "Migma Cell", a complete reactor unit having an estimated power output between 10 mW and 10W. The power output is assumed to be limited by space charge effects, and a subsequently proposed solution to this problem has led Maglich to conclude that a Migma Cell 40 cm in diameter might produce 0.1 megawatts.[3,4] These results are sufficiently impressive to stimulate a more widespread investigation and, at the same time, a more thorough analysis of Migma fusion devices.

Basically, the Migma Cell is a device for storing deuterons (or other ions) in precessing and self-colliding orbits, which loop through the center of an axially symmetric magnetic field. The design of such a device therefore requires, first of all, comprehensive information on the properties of these orbits. In a previous paper, we provided a systematic study of the orbit precession and vertical focusing for ions moving close to the median plane.[5] Here, we shall extend this treatment to the properties of orbits which execute large (nonlinear) vertical oscillations.

Ions moving in an axially symmetric magnetic field have a constant (generalized) angular momentum, $P_\theta = K$, as well as constant energy E. Since the corresponding cyclic coordinates, the azimuth θ and the time t, are not relevant to the properties of a Migma,

the motion of the ions can be characterized by just four phase space coordinates: K, E, and the vertical coordinates z and p_z. Under steady state conditions the distribution of the ions in this four dimensional space will completely specify all of the properties of the Migma.

Any ion which starts on the z-axis (r=0) will have K=0, and its precessing orbit will execute a sequence of loops each of which passes through the z-axis. An example of an orbit with K=0 is shown in fig. 1. The "automatic return" of such orbits to r=0 is a direct consequence of angular momentum conservation. Production of a Migma with its high density central core therefore requires that, under steady state conditions, the ions have an angular momentum distribution which is sharply peaked about K=0.

The properties of the injected beam play a crucial role in determining the eventual steady state distribution of the ions in phase space. The beam should be injected so that its central ray passes through the origin, r=z=0. This central ray will then have K=0, and the angular momentum distribution of the injected ions will be centered on K=0 with an initial spread δK, which should be made as small as possible. The value of δK will depend not only on the horizontal emittance, $(\delta r)(\delta p_r/p)$, but also on the energy spread δE within the injected beam. For example, if the beam is injected at $r=r_{max}$ (as in fig. 1), the contribution to δK from δE is given by:

$$\delta_E K = (r_{max}/v)\delta E. \qquad (1)$$

Other considerations regarding beam injection will be discussed in sec. 5.

All of our orbit calculations in this paper pertain specifically to the important K=0 states, and most of our orbit data will be presented in the form of z vs. p_z/p "phase space diagrams" for a set of relevant p values. Such diagrams can be very useful since they provide a compact representation for a large number of complicated three dimensional orbits (such as those shown by Maglich[2] in his fig. 3). Moreover, because of the occurrence of nonlinear coupling resonances, these diagrams exhibit some rather interesting topological features which reveal important changes in the character of the orbits with increasing vertical amplitude. Finally, such diagrams provide a basis for the direct application of standard phase space concepts and theorems.

2. Equations of motion

The components B_z and B_r of an axially symmetric magnetic field can be derived from a single vector potential component A_θ (r,z). Setting $A_\theta = B_0 A(r,z)$, where B_0 is some field unit, the constant angular momentum K is then given by:

$$K = mr^2(d\theta/dt)+m\omega rA(r,z), \qquad (2)$$

with: $\omega = qB_0/mc$. The frequency ω provides a convenient time unit, and we therefore use $\phi = \omega t$ as a dimensionless time variable.

Following the usual procedure for introducing the "quasi-potential", we obtain the following Hamiltonian $H = H(r,p_r,z,p_z)$ for the radial and vertical motion:

$$H = \tfrac{1}{2}(p_r^2+p_z^2)+\tfrac{1}{2}[(K/m\omega r)-A(r,z)]^2, \qquad (3)$$

where here, $p_r=v_r/\omega$, and $p_z=v_z/\omega$. For the only case of interest to us here, namely K=0, the equations of motion then become:

$$dr/d\phi=p_r,\ dp_r/d\phi=-A(\partial A/\partial r); \qquad (4a)$$

$$dz/d\phi=p_z,\ dp_z/d\phi=-A(\partial A/\partial z); \qquad (4b)$$

and, from eq. (2),

$$d\theta/d\phi=-A/r. \qquad (4c)$$

The orbit data to be discussed in this paper were obtained from programs which integrate these special equations of motion. The constancy of H is used only to check the accuracy of the numerical integration.

Most of our results have been obtained for the same field as used by Maglich[2], namely:

$$B_z=B_0[1+(2z^2-r^2)/R_0^2], \qquad (5)$$

with: $R_o = R/\sqrt{k}$, where k is the "field index" and R is the "field radius", as defined by Maglich. The constant R_0 provides a convenient length unit, and in this case, the function A(r,z) becomes:

$$A = \tfrac{1}{2}r(1+2z^2-\tfrac{1}{2}r^2), \qquad (6)$$

and the specific equations of motion are then obtained directly from (4).

Having introduced the length unit R_0, we utilize the corresponding momentum unit: $p_0 = m\omega R_0 = qB_0R_0/c$. Thus, for example, we have:

$$p_z = v_z/\omega R_0 = mv_z/p_0. \qquad (7a)$$

Instead of the energy E, we use a dimensionless momentum variable p given by:

$$p = v/\omega R_0 = mv/p_0, \qquad (7b)$$

which is then identical to the variable "$p/\sqrt{K}$" used in our previous paper.[5] The use of these dimensionless variables makes the results of our calculations independent of the choice of any particular ion or of any specific values for B_0 and R_0.

An orbit with K = 0 and a given p value is completely specified by only two additional parameters. We have chosen these parameters, z_i and θ_z, from the initial conditions at t=0, as follows:

$$z(0) = z_i,\ p_z(0) = p \sin\theta_z, \qquad (8a)$$

$$r(0) = 0,\ p_r(0) = p \cos\theta_z, \qquad (8b)$$

where the angle θ_z is the same as that used by Maglich when $z_i = 0$.

3. Periodic orbits

The existence and properties of periodic orbits provide essential guidance for the construction of phase space diagrams. The simplest periodic orbit is the median plane equilibrium orbit (EO), which has a periodicity of one loop. The orbit shown in fig. 1, for example, is the EO for p=0.20. The properties of these orbits were described in detail in our previous paper.[5] In particular, the values obtained for the vertical focusing frequency ν_z (in oscillations per loop) can be summarized as follows:

$$0<p<0.215 \rightarrow 0<\nu_z<0.5; \tag{9a}$$

$$0.215<p<0.253 \rightarrow \nu_z=0.5\pm i\nu_z^*,\ 0<\nu_z^*<0.11; \tag{9b}$$

$$0.253<p<0.268 \rightarrow 0.5<\nu_z<1.0; \tag{9c}$$

where the complex values of ν_z in (9b) indicate that the linear oscillations are unstable. The maximum p value which can be confined in the median plane of this field is $p_{max}=0.272$, and in the narrow range $0.268<p<0.272$, the values of ν_z are mainly complex.

For any "mirror" field, such as the one being considered here, the frequency ν_z generally decreases as the amplitude of the vertical oscillations increases. If Z denotes some average amplitude of these oscillations, we can therefore write:

$$\nu_z(Z)<\nu_z(0), \tag{10}$$

where $\nu_z(0)$ is now the frequency of the strictly linear oscillations given in (9) above. This means, for example, that

all three dimensional orbits for $p<0.215$ will have $\nu_z(Z)<0.5$, as follows from (9a).

In the case of a periodic orbit with a periodicity of n loops, the values of z_i and θ_z in (8) will be the same at the beginning and end of these n loops. If the orbit executes n' oscillations during this period, then we have:

$$\nu_z(Z) = n'/n, \tag{11}$$

for this orbit. We have investigated periodic orbits with $n\leq 10$, and for a given n value the restriction (10) specifies the possible n' values.

Using a special computer program, we have calculated the properties of all significant periodic orbits for particular p values of interest. For example, for p=0.20, where $\nu_z(0)=0.385$, we have found periodic orbits with: $\nu_z(Z)=3/8$, 2/6, 3/10, 1/4, 2/10, and 1/6, in order of increasing Z value. Fig. 2 shows plots of z versus r for the two different orbits having $\nu_z=1/4$, the simplest of these many orbits. When plotted in the rz-plane, all of these orbits appear somewhat like Lissajous figures.

A particular periodic orbit may be either "stable" or "unstable". It will be stable if for a small change in initial conditions, the resultant displaced orbit simply oscillates about the given periodic orbit; otherwise, it will be unstable. Stable periodic orbits can be easily recognized, and in the process of verifying the sample orbit data provided by Maglich[2], we uncovered two examples. The orbit in his fig. 2, which we find to have

p=0.224 in our units, executes a small oscillation about the ν_z=1/2 periodic orbit; the orbit in his fig. 3 with θ_z=40° turns out to have p=0.18 and oscillates about the ν_z=1/6 periodic orbit. These results confirm our previous conjectures concerning these orbits.[5]

In order to analyze the stability of the periodic orbits, it is necessary to consider linear displacements η and ζ, defined by:

$$r \to r+\eta, \quad z \to z+\zeta, \tag{12}$$

and to find the differential equations for η and ζ from those for r and z given in eq. (4). Since the resultant η and ζ equations are coupled, it is therefore necessary to construct a general 4x4 transfer matrix following a procedure discussed by Kolomensky and Lebedev.[6] We have carried through this process and have calculated the resulting four eigenvalues of the transfer matrix. We find that one pair of these eigenvalues is always +1, and that the other pair is given by: $\exp(\pm i\mu)$. Specifically, we compute $\cos\mu$ for a given periodic orbit, and can therefore readily determine whether it is stable or unstable, and to what degree. As an example, for the two orbits with ν_z=1/4 shown in fig. 2, the stable one (solid curve) has $\cos\mu$ = -0.87, while the unstable one (broken curve) has $\cos\mu$ = 4.53.

Of all the periodic orbits, the stable orbit with ν_z=1/2 is unique in that it passes through the origin once per loop, just like the median plane equilibrium orbit (EO). Such orbits may therefore have special significance for a Migma. As noted

above, the ν_z=1/2 orbit cannot exist for p<0.215 where $\nu_z(0)$<0.5. Fig. 3 shows z versus r plots for these ν_z=1/2 orbits for p=0.23, 0.26, and 0.29. As indicated by these plots, this orbit grows out of and away from the EO as p rises above 0.215. Our data for these ν_z=1/2 orbits show that the horizontal precession angle θ_p decreases as p increases; for example, we find: θ_p = 24.7 deg/loop and 16.3 deg/loop, at p=0.23 and 0.29, respectively. This precession behavior contrasts with that for the EO where θ_p always increases with p, as we have shown before.[5]

Periodic orbits generally occur in pairs, one stable and the other unstable. The unstable "mate" of the ν_z=1/2 orbit discussed above coincides with the EO for 0.215<p<0.253, as indicated by (9b) above; it then departs from the EO for p>0.253, always crossing the z-axis (r=0) with p_z=0, and with a value of |z| which increases with p. In the rz-plane, these orbits have a ">" shape with the vertex at $r=r_{max}$, z=0. Although the details will be omitted here, we have also calculated the properties of other pairs of periodic orbits as a function of p.

We should note here that periodic orbits like those described above are usually associated with, and named after, certain nonlinear coupling resonances. For example, the stable and unstable orbits with ν_z=1/2 can be correlated with the $\nu_r=2\nu_z$ nonlinear coupling resonance, as discussed in our previous paper.[5] However, we have not pursued these correlations any further, and we shall continue to identify the periodic orbits simply from their ν_z values.

4. Phase space diagrams

The importance of phase space diagrams has been described at the end of sec. 1. Given a set of orbits for a fixed p value (and K=0), we construct the relevant phase space diagram by plotting z vs. p_z/p once per loop at r=0, and then connecting the points for each orbit. Where the vertical motion is linear and stable, the resultant diagram will show a set of characteristic ellipses centered at $z=p_z=0$ (EO), and differing only by a scale factor which is proportional to the oscillation amplitude Z. For a given orbit, the sequence of plotted points will move around the ellipse with an average angular separation of $2\pi\nu_z$ rad/loop. When ν_z is complex, as in (9b), the linear motion is unstable, and the characteristic ellipses are replaced by hyperbolas all having common asymptotes which pass through $z=p_z=0$, and along which successive points move either outward or inward.

As the oscillation amplitude Z increases, nonlinear effects change the shape of the phase space ellipses and also cause $\nu_z(Z)$ to decrease, as indicated in (10) above. For an orbit starting at r=z=0 with a large θ_z value in the field (5) under consideration here, we have used the "WKB" approximation to obtain an analytical solution of the equations of motion (4), which should be valid when $(2p\cos\theta_z)^2 \ll 1$. Our results show that:

$$(p_z/p)_{max} = \sin\theta_z,\ Z=z_{max}=(R_0/\sqrt{2})\tan\theta_z, \qquad (13a)$$

specify the axes of the ellipse, and that:

$$\nu_z(\theta_z) = (p/\sqrt{2})[\cos\theta_z/(1+\tfrac{1}{2}\tan^2\theta_z)]. \qquad (13b)$$

Thus, as θ_z (or Z) increases, the phase space ellipse tends to become relatively tall and narrow, while the value of ν_z decreases rapidly.

The foregoing discussion describes the features of the phase space diagram only for very small or for very large vertical oscillations. In the intermediate region, the topology is usually determined by the set of periodic orbits discussed in the preceding section. Such an orbit with $\nu_z=n'/n$ will appear in the phase space diagram simply as n discrete "stable fixed points" or "unstable fixed points", depending on whether the orbit is stable or unstable. For example, the stable and unstable orbits with $\nu_z=1/4$ shown in fig. 2 appear as four stable and four unstable fixed points, respectively, in the phase space diagram of fig. 4 discussed below.

Recalling the analogy between incompressible fluid flow and the motion of points in phase space, we can recognize that each stable fixed point acts like the center of a local "vortex". Also, to preserve continuity of "flow", each vortex must be bounded by a "separatrix curve" which emanates from the associated unstable fixed points. When the separatrix curves are drawn in the phase space diagram, the n vortex regions so defined appear like a ring of n "sausages", as will be seen below. We have calculated the separatrix curves for the important fixed points in our phase space diagrams; however, these curves become poorly defined when the unstable orbit has a very large cosμ value.

Phase space diagrams will be presented here for p=0.20, 0.23, and 0.26, one for each of the three ν_z regions given in (9a,b,c) above. The higher p values are most important

since they correspond to larger ν_z values, and hence to better vertical confinement for a Migma. Also, if an electrostatic inflector is used for injection, the higher p values will simplify its design. Finally, these p values are consistent with both the orbit data supplied by Maglich[2] and the data for his Migma Cell design, where p ranges between 0.18 and 0.27, in our units (7).

Fig. 4 shows the phase space diagram for p=0.20, where $\nu_z(0)=0.385$. Reading from the center outward, the points and curves represent data for: $\nu_z(Z)=3/8$, 2/6, 3/10, 1/4, 2/10, and 1/6, in order of increasing Z. The stable fixed points (circles) and unstable fixed points (dots), together with the separatrix curves, are shown for $\nu_z=1/4$ and 2/6. Because $\nu_z=1/4$ corresponds to a lower order nonlinearity than $\nu_z=2/6$, the four vortex regions of the former are significantly larger than the six vortex regions of the latter. For $\nu_z=1/6$, the diagram shows only the six stable and six unstable fixed points connected by a broken curve, since the vortex regions are quite insignificant in this case. The remaining three solid curves in the diagram represent the data points for $\nu_z=3/8$, 3/10, and 2/10. For larger Z values than those shown in this diagram (and those below), we find that formulas (13a,b) provide a good representation of the data.

Fig. 5 shows the phase space diagram for p=0.23, where $\nu_z(0)$ is complex, as indicated in (9b). Here, the EO is the unstable periodic orbit for $\nu_z=1/2$, as noted in sec. 3. The corresponding point $z=p_z=0$ in the diagram is therefore an unstable fixed point, and the "propeller-shaped" separatrix

curve emanating from this point goes around the two stable fixed points (circles) which correspond to the stable orbit for $\nu_z=1/2$ shown as the curve "a" in fig. 3. Outside of these two vortex regions are plots representing the data for $\nu_z(Z)=4/10$, 3/8, 2/6, 1/4, and 2/10, in order of increasing Z. For $\nu_z=1/4$ and 2/6, the vortex regions and separatrix curves are directly analogous to those shown in fig. 4. Here again, three solid curves are used to represent the remaining data for $\nu_z=4/10$, 3/8, and 2/10.

Fig. 6 shows the phase space diagram for p=0.26, where $\nu_z(0)=0.683$. The "propeller-shaped" separatrix curve in fig. 5 has now evolved into a "bowtie-shaped" curve emanating from the two $\nu_z=1/2$ unstable fixed points located at $z=\pm 0.12$, $p_z=0$. The "knot" of the bowtie corresponds to the vortex region surrounding the EO, and contains close to its center a solid curve passing through the $\nu_z=4/6$ data points. The "wings" of the bowtie represent the vortex regions around the two $\nu_z=1/2$ stable fixed points, which correspond to the orbit labelled "b" in fig. 3. Next, outside the bowtie, lies a broken curve connecting the twelve fixed points for $\nu_z=2/6$ which are now all unstable; between p=0.23 and 0.26, the six stable fixed points undergo "fission" into six unstable points (shown as small dots) and 12 stable points (not shown). Next in the diagram, lie the remnants of the $\nu_z=1/4$ vortex regions which are so prominent in the previous two figures; each of the four previously stable fixed points has undergone "fission" twice between p=0.23 and 0.26, so that each has degenerated into three unstable (small

dots) and four stable (circles) fixed points, which are shown in the diagram loosely connected by a broken curve to the original four unstable points (large dots). The outermost solid curve in the diagram represents the data for $\nu_z=2/10$. This phase space diagram appears rather disordered when compared with those in fig. 4 and fig. 5, and the progression from relative order to disorder results from the fact that as p increases here, the orbits extend further out into the rapidly changing edge region of the field.

Although the phase space diagrams described above pertain specifically to the somewhat unrealistic field (5), the basic features of these diagrams should be the same for any other "mirror" field, for which B_z increases along the z-axis with increasing distance $|z|$ from the median plane. We have verified this conclusion for one other, quite different field, namely that produced by a pair of very small (dipole) coils. For a realistic field, however, B_z will reach a finite maximum value, $(B_z)_{max}=B_z(z_0)$, at some distance $|z| = z_0$. An orbit starting at r=z=0 with a large θ_z value will be confined by this realistic field only if $\theta_z \leq \theta_z^{max}$, where θ_z^{max} is given approximately by the "loss cone" formula:

$$\cos^2\theta_z^{max} = B_0/B_z(z_0). \qquad (14)$$

This formula is quoted in the paper by Maglich, et al.[1], and is used (though somewhat incorrectly) by Maglich[2] in obtaining his eq. (13) for Δz.

The above confinement limit implies that the actual $\nu_z(\theta_z)$ decreases faster than predicted from eq. (13b), and indeed

that $\nu_z(\theta_z)\to 0$ when $\theta_z\to\theta_z^{max}$. Moreover, this confinement limit implies that the operational boundary of a phase space diagram will be established by an outermost separatrix curve which emanates from two unstable fixed points located at $z=\pm z_0$, $p_z=0$, and which passes through the points z=0, $p_z/p=\pm\sin\theta_z^{max}$. That is, any orbit starting at a point outside this boundary curve will eventually exit from the operational region of the field. In order to limit multiple scattering losses in his Migma Cell, Maglich has assumed $\theta_z^{max} > 55°$, and in this case, the outermost boundary curve would lie outside and enclose the area of the phase space diagram shown in our figs. 4-6.

5. Beam injection

Beam injection poses difficult problems for a continuously operating Migma device. The injection scheme proposed by Maglich[2] in sec. 13 of his paper depends for its success on a "self-ensaring" mechanism. Using a conventional inflector, deuterons would be injected into precessing and self-colliding orbits, and the multiple scattering which then ensues would prevent (or at least inhibit) the ions from returning to strike the inflector. Thus, the ions would be self-ensnared. In an alternative version of this scheme, a beam of molecular ions D_2^+ would be injected, and the self-dissociation of these ions in the Migma core would produce captured deuterons. This latter method is currently being used in an experimental device.[7]

The injected beam will be characterized by a certain vertical emittance, $(\delta z)(\delta p_z/p)$, which will translate into an equal area of the phase space diagram at r=0, like one of those shown in

our figs. 4-6. Ordinarily, the injected beam would be centered on a median plane equilibrium orbit (EO), or on one of the $\nu_z=1/2$ stable periodic orbits shown in fig. 3. Either choice would maximize the resultant spatial density $\rho_i(r,z)$ of the injected ions at r=z=0, which seems essential to the proper formation of a Migma. These injected ions would, however, soon return to strike the inflector electrode. For example, the EO shown in fig. 1 for p=0.20 has a precession angle $\theta_p=21.6$ deg/loop, and would close on itself almost perfectly after 50 loops, while missing by $\delta\theta=7.2°$ after 17 and 33 loops. Similarly, the $\nu_z=1/2$ orbit shown in fig. 3 for p=0.23 has $\theta_p=24.7$ deg/loop.

Maglich has suggested that the time required for the injected ions to return to the inflector position could be greatly extended by injecting the beam off the median plane with a resultant large coherent vertical oscillation. However, this would invariably produce a much lower density ρ_i at r=z=0, which would by itself be rather disadvantageous for self-ensnaring.

A possible way out of this dilemma is suggested by the "propeller-shaped" separatrix curve at the center of fig. 5, which passes through the unstable fixed point at $z=p_z=0$, the EO. Theoretically, an ion orbit starting exactly on this curve, at a point corresponding to the "tip of the propeller blade", requires an infinite number of loops to reach $z=p_z=0$, since it approaches this point (the median plane) asymptotically. Fig. 7 shows a z vs. r plot for the first eight loops of this proposed injection orbit, or one very close to it. If the injected beam is centered on this orbit, the ion distribution will very quickly cover the entire separatrix curve plus a small adjoining region

in the phase space. Not only will a very long time be required for these ions to return to the inflector position, but most of this time will be spent close to the median plane, so that nearly the maximum possible density ρ_i will be achieved at r=z=0. It should be noted, however, that the $z=p_z=0$ fixed point is quite unstable, so that ions which are injected slightly off the separatrix curve will make a complete circuit around this curve and return to the starting point in a surprisingly small number of loops. We find, for example, that an orbit which misses the separatrix curve by only 1.0 millirad will complete the circuit in just about 26 loops. Nevertheless, this number is still very large compared to the normal period of the vertical oscillations, $1/\nu_z$.

If deuterons themselves are injected, then the success of self-ensnaring depends on multiple scattering for removing ions from the initial phase space volume occupied by the injected beam. However, because the inflector is an extended obstacle, the total phase space volume for orbits which can strike this obstacle is very much greater than the initial volume. Moreover, multiple scattering can, at a crucial moment, transfer an ion into as well as out of the critical phase space volume. We should also note that the inflector constitutes an asymmetric element in the system, and the effect of its fringe field will tend to move the ion orbits away from the magnetic field axis (r=0), and hence diminish the central Migma density.

The alternative self-ensnaring scheme suggested by Maglich involves the injection of D_2^+ molecular ions, as noted above. Here, the dissociation reactions yield: $p(D^+) \approx \frac{1}{2} p(D_2^+)$, so that the captured deuterons would be restricted to relatively low momenta, and hence small ν_z values. For example, if the D_2^+ ions are injected on an orbit like that shown in fig. 7, then we must require that $p(D_2^+)<0.25$, which leads to $p(D^+)<0.13$ and $\nu_z<0.18$. Also, as indicated in our discussion regarding fig. 6, we find that values of $p(D_2^+)>0.25$ are unlikely to provide the injected ions with either the favorable orbits or the extended confinement time required for efficient deuteron production.

6. Multiple scattering and core density

Multiple Coulomb scattering between the self-colliding ions transforms the initial phase space distribution of the injected beam into the final distribution characterizing the steady state of the Migma. Qualitatively speaking, multiple scattering acts like a "random walk" process in phase space which causes the points representing the ions to diffuse outward and away from the compact phase space volume they initially occupy. This diffusion continues until a steady state condition is achieved; that is, until: $I_{in}=I_{out}=I_{fusion}+I_{lost}$, where I denotes ions/sec.

Some qualitative aspects of the steady state distribution can be inferred from the phase space diagrams shown in figs. 4-6. For example, we can expect the major unstable fixed points in these diagrams to become local minima in the density, since phase space trajectories are "repelled" by these points. Conversely,

the important stable fixed points (vortex centers) should develop into positions of local maxima in the density. For $p>0.25$, the topology changes drastically as can be seen in fig. 6 for $p=0.26$; here, the vortex regions have become fragmented through a multiplication of the fixed points. We also find in this case that the density of points close to the p_z-axis has become relatively low, which implies a corresponding low spatial density $\rho(z)$ near $z=0$ in the Migma core. For the Maglich field (5) used in these calculations, $p_{max}=0.272$ is the momentum confinement limit for motion in the median plane with $K=0$, and it should therefore not be surprising that the quality of the phase space diagrams deteriorates as $p \to p_{max}$. Since multiple scattering also produces a diffusion spread in the momentum (or energy) of the ions, the injection momentum p_i should be chosen sufficiently far below p_{max} so as to avoid any significant leakage of ions into the momentum region with unfavorable phase space diagrams.

Miller[8] has carried out multiple scattering calculations appropriate to a Migma on the assumption that the vertical oscillations are all simple harmonic oscillations with a constant frequency. His assumed phase space diagrams are therefore quite different from those shown in our figs. 4-6. In particular, his analysis overlooks the significant decrease in ν_z with increasing θ_z. The method used by Miller should nevertheless be valid for small θ_z values, when $p<0.2$.

In order to limit multiple scattering losses, Maglich[2] assumes (at the end of sec. 19 in his paper) that $\theta_z^{max} > 55°$,

and as noted at the end of sec. 4, the phase space diagrams change character as $\theta_z \to \theta_z^{max}$. For the special field (5) under consideration here, eq. (13) describes the phase space ellipse at r=0 when θ_z is large. In addition, our analytical result shows that the relative number of points on this ellipse near z=0 decreases rapidly as θ_z increases. That is, if $F_1(\theta_z)$ is the fraction of points with $|z| \le z_1$ at r=0, then for a given z_1, we find:

$$F_1(\theta_z) = (2\sqrt{2}/\pi)(z_1/R_0)[\cot\theta_z/(1+\tfrac{1}{2}\tan^2\theta_z)], \qquad (15)$$

provided $(z_1/R_0)^2 << \frac{1}{2}\tan^2\theta_z$, and $(2p\cos\theta_z)^2 << 1$. This $F_1(\theta_z)$ can be interpreted as the probability of finding the ion inside the core with $|z| < z_1$. For a more realistic field, the value of F_1 would actually go to 0 as $\theta_z \to \theta_z^{max}$.

We can use the above formula to obtain some qualitative information about the variation of the ion density $\rho(z)$ in the Migma core (r=0). First, if we take $\theta_z^{max} = 55°$, then eq. (14) yields: $B_z(z_0) \simeq 3.0\ B_0$, and the core will extend out to a distance z_0 from the median plane. Using the field (5) to obtain an estimate for z_0, we find:

$$z_0 = (R_0/\sqrt{2})\tan\theta_z^{max} \simeq 1.0 R_0, \qquad (16)$$

in agreement with (13a). This means that the full vertical height of the core would be $2z_0 \simeq 11$ cm in the field used by Maglich in his Migma Cell design, where $R_0 = R/\sqrt{K} \simeq 5.6$ cm.

Let us assume now that $\rho(z)$ is sharply peaked at z=0, and rapidly becomes very small for $|z| > z_1 = 0.1R_0$, which

corresponds roughly to $\theta_z > 10°$. This is equivalent to assuming that the steady state density $\rho(z)$ does not differ substantially from the density $\rho_i(z)$ for the injected ions discussed in the preceding section. Such an assumption seems quite compatible with Maglich's description of the Migma and its core. Thus, if we take $z_1/R_0 = 0.1$, then we obtain from eq. (15) the following probabilities for finding an ion inside the high density region of the core: $F_1 = 0.13$ for $\theta_z = 30°$, and $F_1 = 0.06$ for $\theta_z = 45°$. These very small probabilities imply that ions with $\theta_z \gtrsim 25°$, rather than 55°, would be effectively "lost" from participating in the fusion reactions. Also, the multiple scattering rate would be very much greater for the ions in the high density region ($\theta_z < 10°$) than for those outside this region ($\theta_z > 25°$), so that the outward diffusion of the former would far outweigh the outward diffusion of the latter.

We can, for example, reinterpret the numerical results given by Miller[8] to show that the time required for an injected ion to diffuse out of the high density region would be: $\tau_v(\theta_z \to 10°) \simeq 200$ sec, which is comparable to the "fusion time", 50 sec, given by Maglich[2] in his eq. (45). Moreover, for the core density $\rho(z)$ assumed above, an extension of Miller's analysis to include $F_1(\theta_z)$ of eq. (15) would yield an almost infinite result for $\tau_v(\theta_z \to \theta_z^{max} = 55°)$, the diffusion time for an ion to reach the confinement limit. Under these conditions, about 20% of the injected ions would continuously diffuse out from the high density region into the low density region, where they would remain, thereby increasing the density in the outer region.

We must therefore conclude that the sharply peaked density function $\rho(z)$ assumed above would not be consistent with steady state conditions. It therefore seems quite likely that $\rho(z)$ falls off much more gradually with increasing $|z|$ out to z_0, the confinement limit. In this case, a significant fraction of the ions will be distributed over a wide area of the phase space diagram under steady state conditions. Unfortunately, such a widespread distribution requires a much more complicated analysis to evaluate the important reaction parameters, $\langle \sigma v_{12} \rangle$, for fusion and for multiple scattering.

References

1. B. C. Maglich, J. P. Blewitt, A. P. Colleraine, and W. C. Harrison, Phys. Rev. Lett., 27(1971)909.
2. B. C. Maglich, Nucl. Instr. and Meth., 111(1973)213.
3. R. A. Miller, Nucl. Instr. and Meth., 119(1974)275.
4. B. C. Maglich and R. A. Miller, Bull. Am. Phys. Soc., 18 (1973)1322, abstr. 5All.
5. M. M. Gordon and D. A. Johnson, Nucl. Instr. and Meth., 121 (1974)461.
6. A. A. Kolomensky and A. N. Lebedev, Theory of Cyclic Accelerators, (North Holland Publ., Amsterdam, 1966) ch. 2, sec. 3.
7. B. C. Maglich, et al., Nucl. Instr. and Meth., 120(1974)309.
8. R. A. Miller, Phys. Rev. Lett., 29(1972)1590.

Figure Captions

Fig. 1. XY-plot of the median plane equilibrium orbit for p=0.20. This precessing orbit repeatedly loops through the center of the axially symmetric magnetic field. For this and subsequent figures, we use the length unit R_0 and the momentum unit $p_0=qB_0R_0/c$ defined by the field parameters in eq. (5).

Fig. 2. z vs. r plots of the stable (solid curve) and unstable (broken curve) periodic orbits with $\nu_z=1/4$ at p=0.20. These two orbits appear simply as four stable and four unstable fixed points, respectively, in the phase space diagram of fig. 4.

Fig. 3. z vs. r plots of the stable periodic orbits with $\nu_z=1/2$ for: (a) p=0.23, (b) p=0.26, and (c) p=0.29. The two orbits labelled "a" and "b" each appear as two stable fixed points in the phase space diagram of fig. 5 and fig. 6, respectively.

Fig. 4. Phase space diagram showing plots of z vs. p_z/p at r=0 constructed from orbit data for p=0.20. Reading from the center outward, the points and curves represent schematically the orbit data with: ν_z=3/8(C), 2/6(SUV), 3/10(C), 1/4(SUV), 2/10(C), and 1/6(SUB), with the following notation: C=solid curve; S=stable fixed points (circles); U=unstable fixed points (dots); V=vortex regions bounded by separatrix curves (solid); B=broken curve.

Fig. 5. Phase space diagram for p=0.23, analogous to that shown in fig. 4. Reading from the center outward, orbit data are shown for: ν_z=1/2(SUV), 4/10(C), 3/8(C), 2/6(SUV), 1/4(SUV), and 2/10(C), using the notation adopted in fig. 4. The "propeller-shaped" separatrix curve at the center of this diagram corresponds to the proposed injection orbit shown in fig. 7.

Fig. 6. Phase space diagram for p=0.26, analogous to those shown in fig. 4 and fig. 5. Reading from the center outward, orbit data are shown for: ν_z=4/6(C), 1/2(SUV), 2/6(UuB), 1/4(SUuB), and 2/10(C), using the notation adopted for fig. 4 with the following addition: u=minor unstable fixed points (small dots).

Fig. 7. Plot of z vs. r for the first eight loops of a proposed injection orbit for p=0.23. This orbit starts from $r=r_{max}$, $z=z_{max}$, at the point labelled "0", and reaches in succession the points labelled "1,2,3" at the end of its first three loops. Subsequent loops are unmarked, and to avoid overplotting, further loops beyond the first eight are not shown. An ion in this orbit would evidently spend most of its time close to the median plane. Note that the z scale interval is twice that of the r scale here. See also fig. 5.

Fig. 1

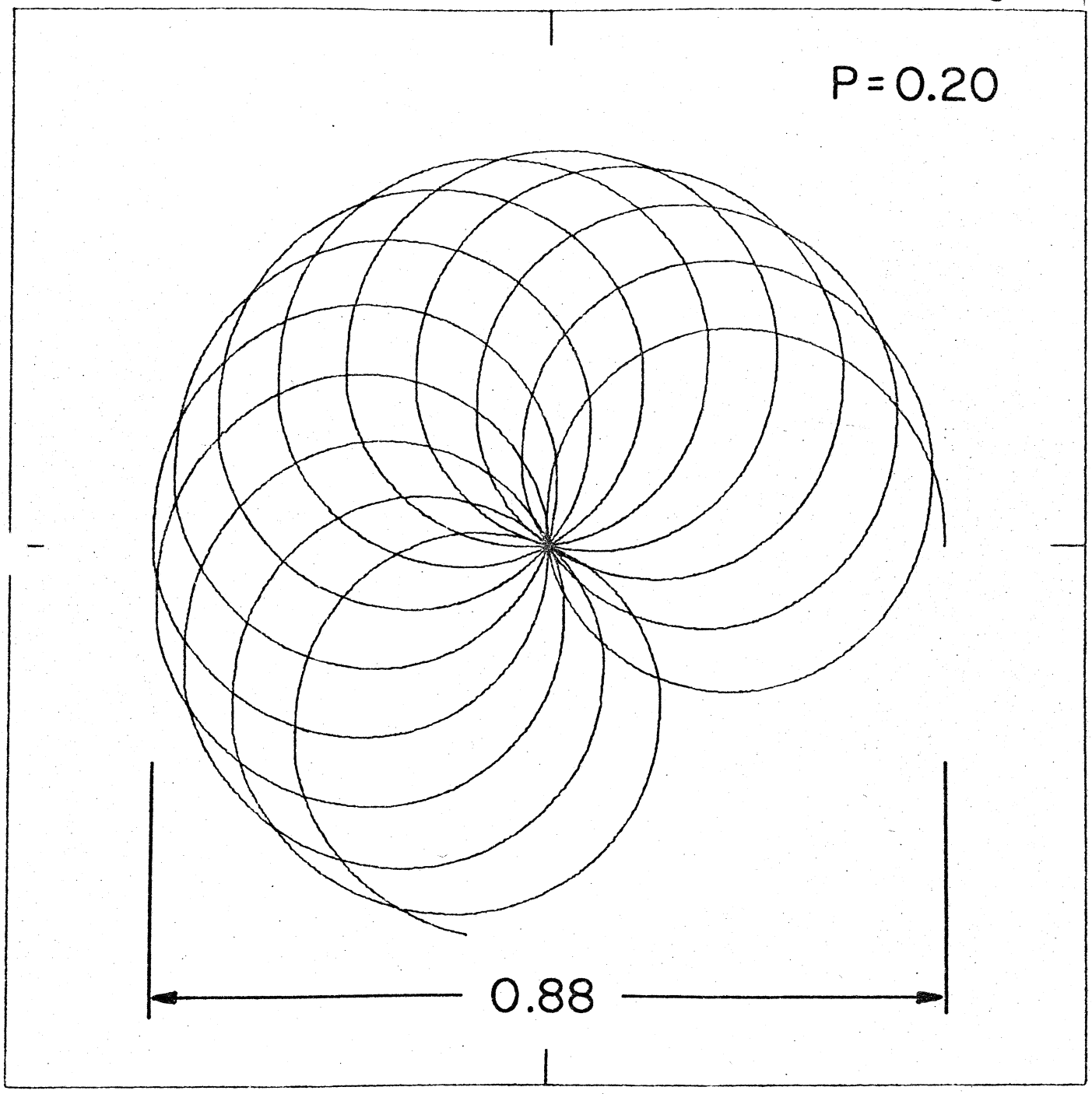

Fig. 2

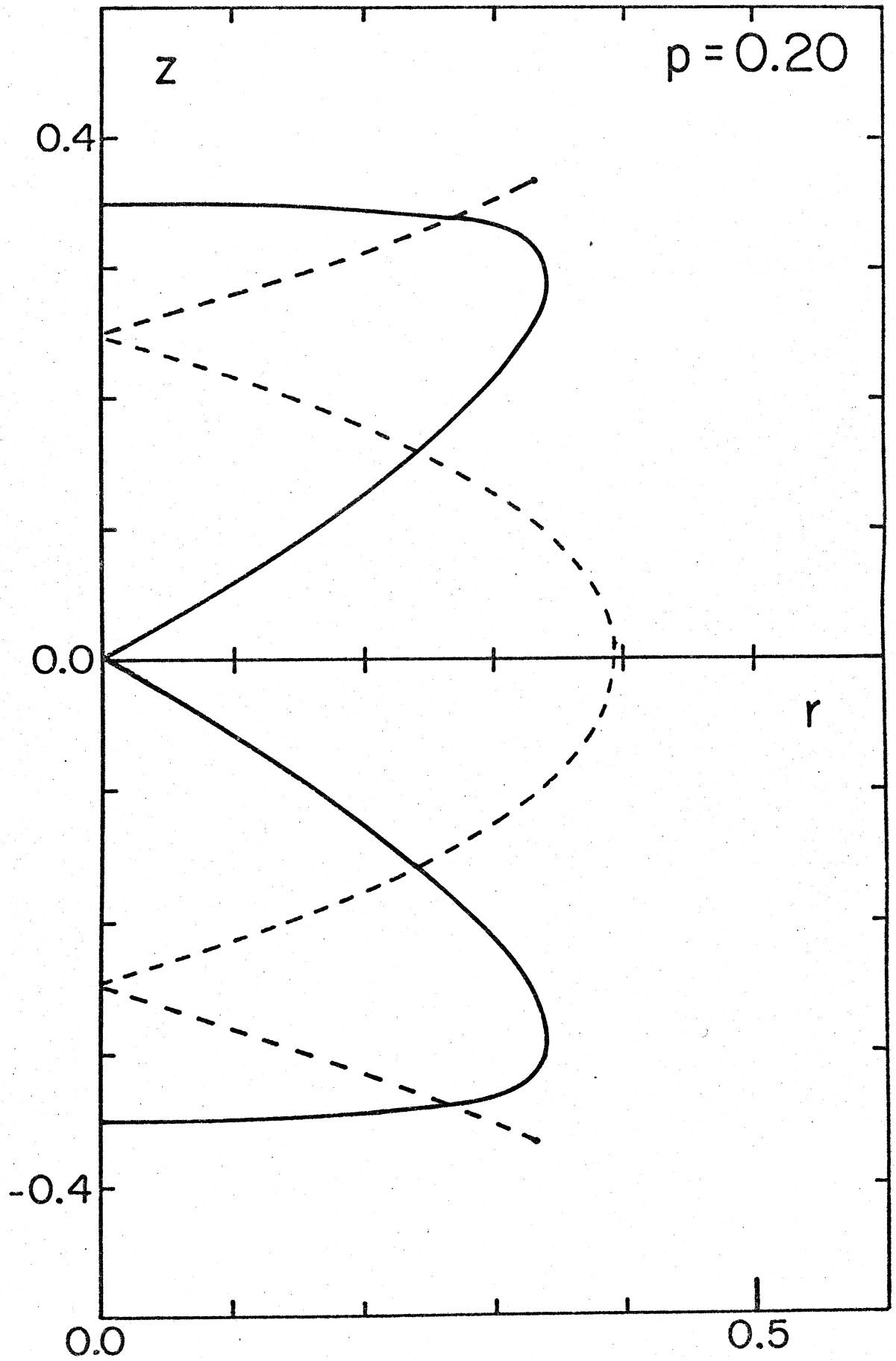

Fig. 3

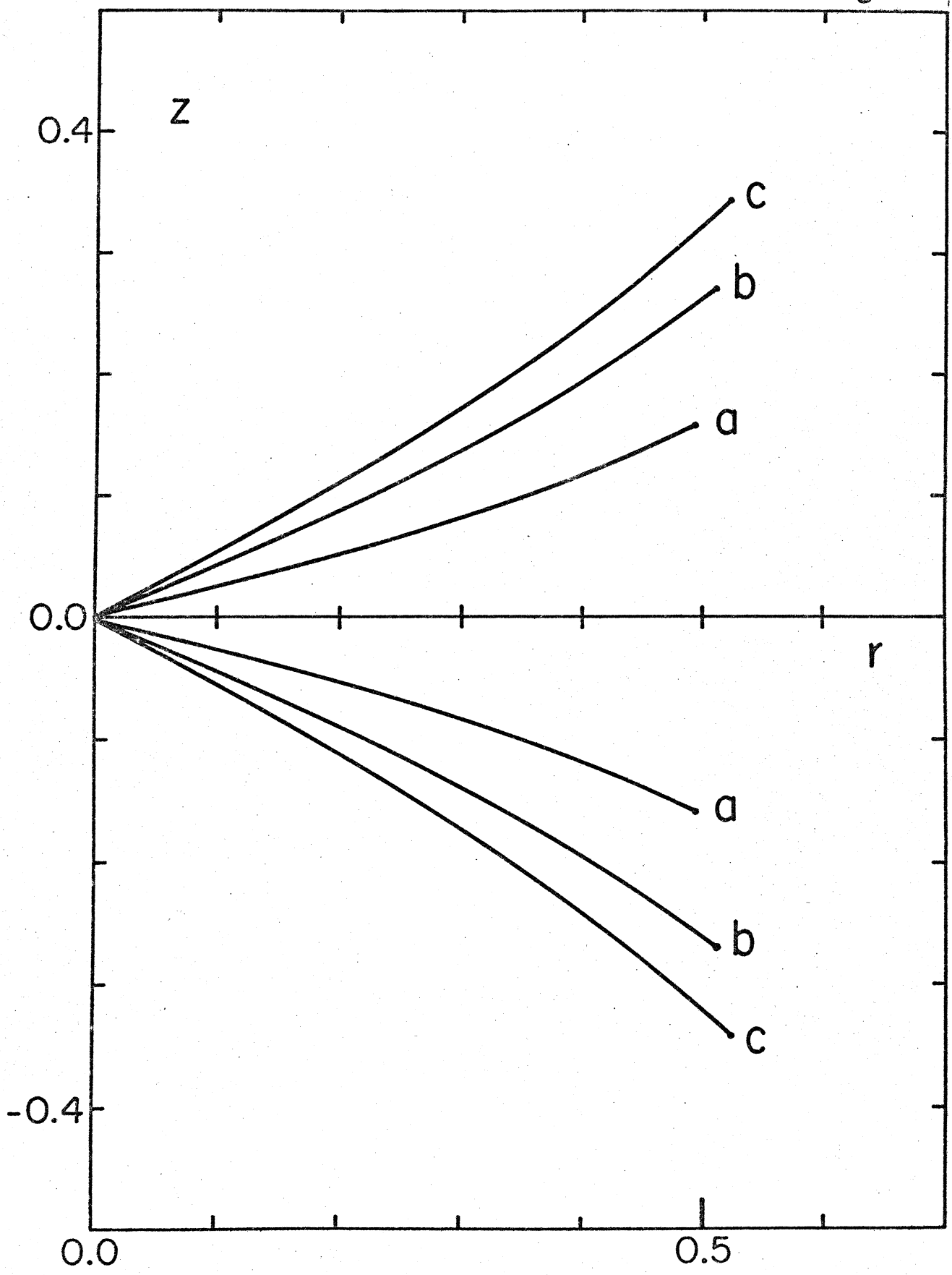

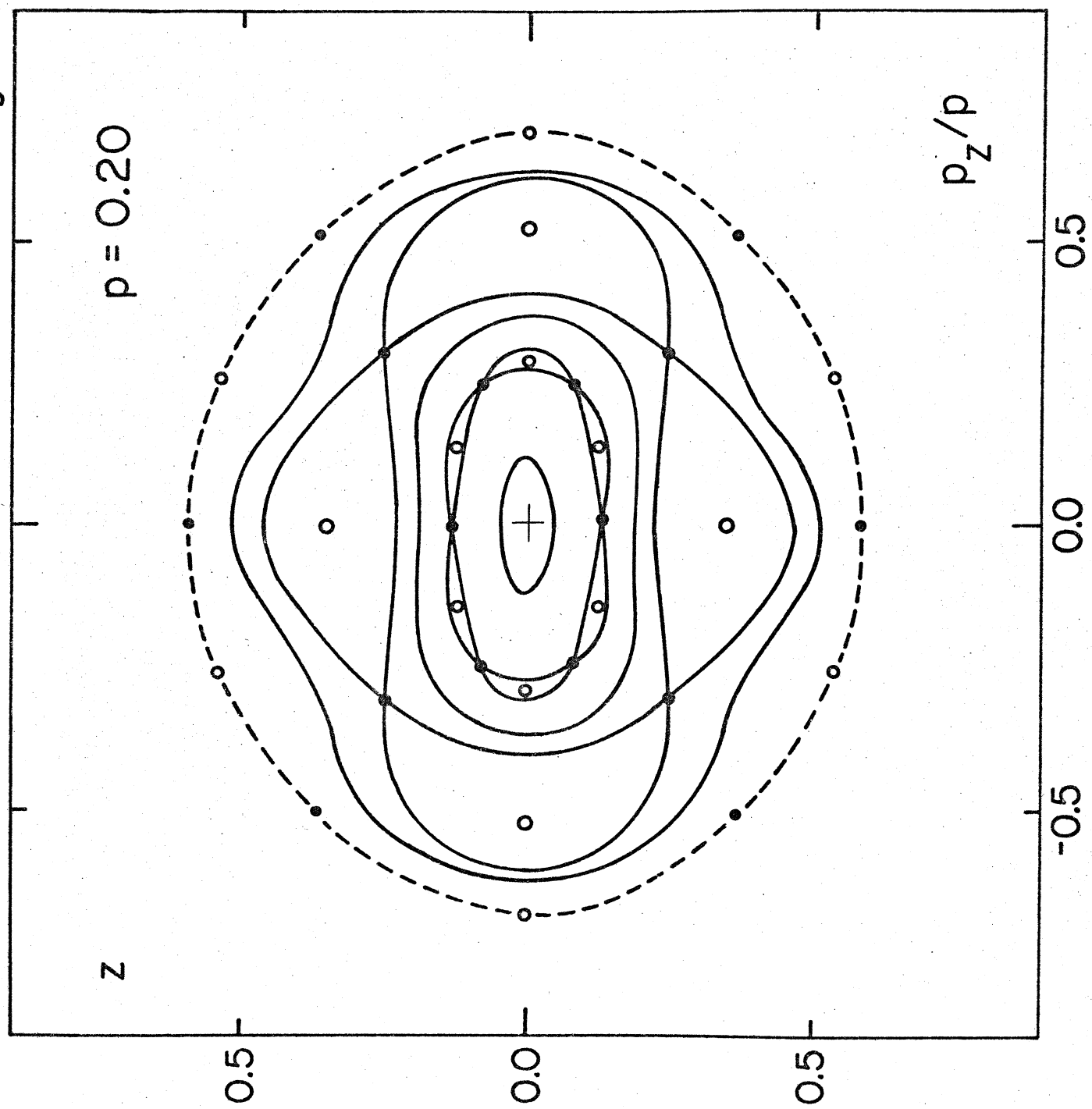

Fig. 4

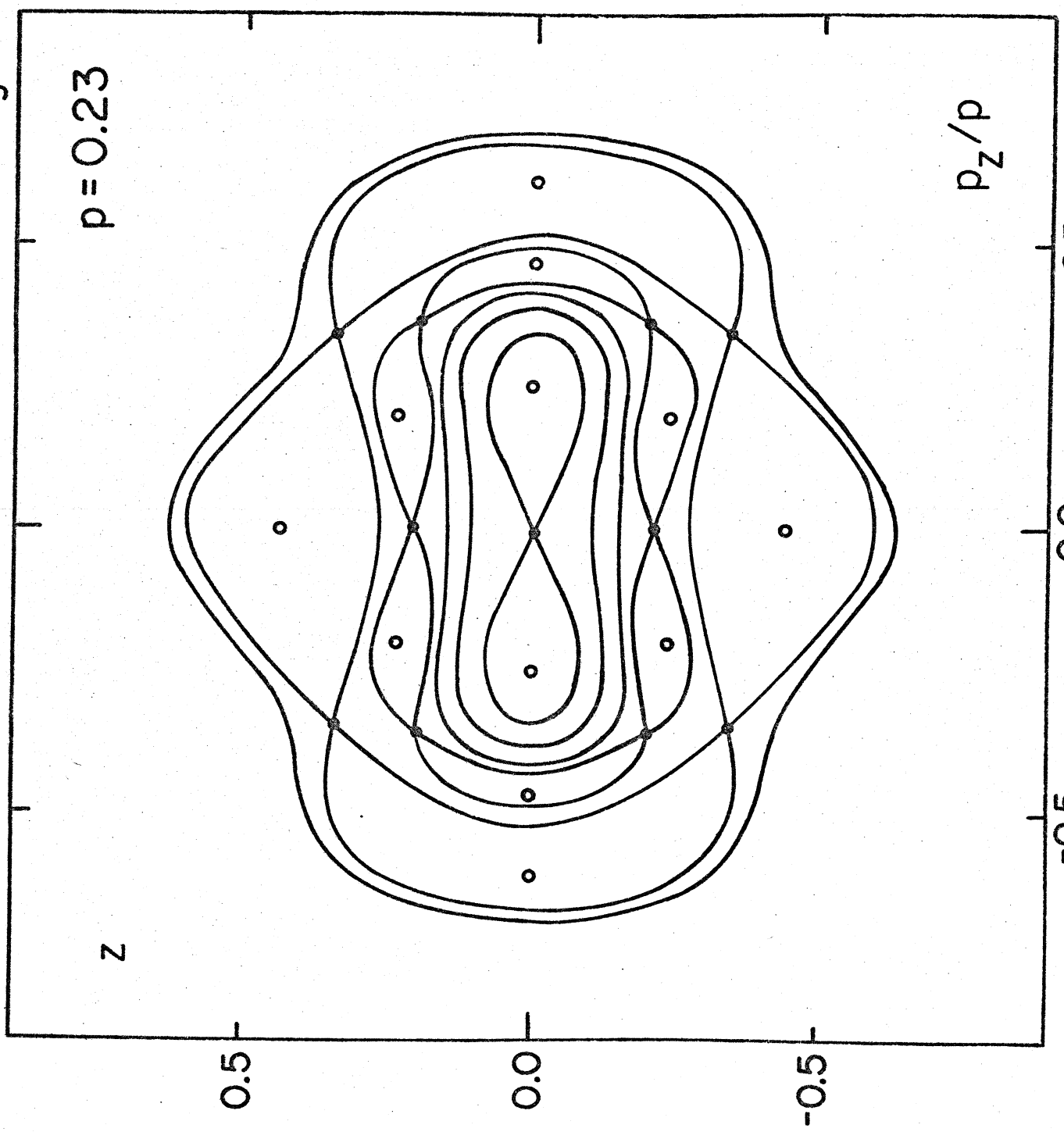

Fig.5

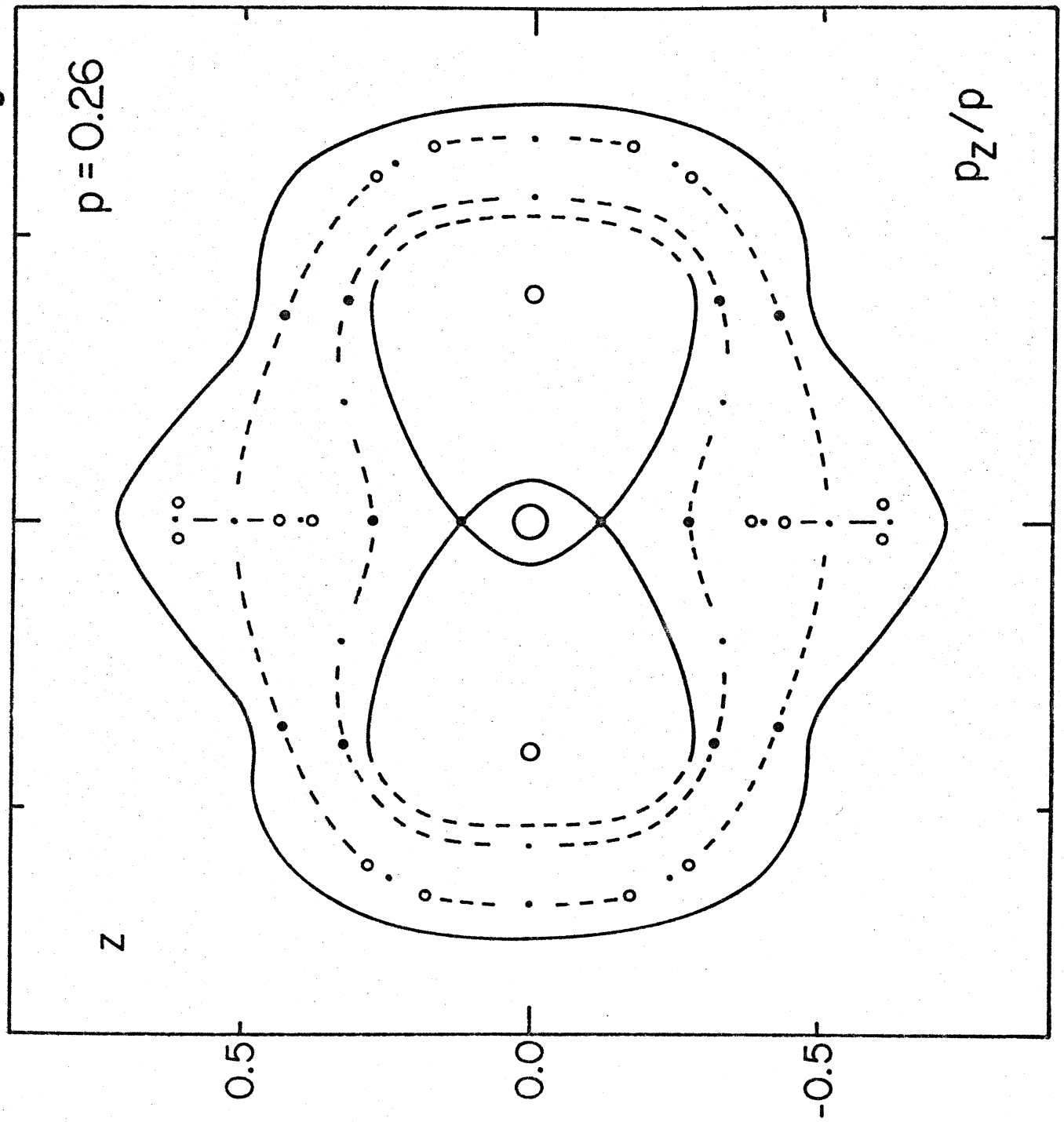

Fig.6

Fig. 7